Petroleum Science 19 (2022) 2781–2795

Contents lists available at ScienceDirect

Petroleum Science

journal homepage: www.keaipublishing.com/en/journals/petroleum-science

Original Paper

# Numerical simulation of fracture propagation in Russia carbonate reservoirs during refracturing

Dao-Bing Wang [a, *], Fu-Jian Zhou [b], Yi-Peng Li [c], Bo Yu [a, **], Dmitriy Martyushev [d, ***], Xiong-Fei Liu [b, ****], Meng Wang [e], Chun-Ming He [e], Dong-Xu Han [a], Dong-Liang Sun [a]

[a] School of Mechanical Engineering, Beijing Institute of Petrochemical Technology, Beijing, 102617, China
[b] Unconventional Oil and Gas Science and Technology Research Institute, China University of Petroleum-Beijing, Beijing, 102249, China
[c] Tuha Downhole Service Company of Xibu Drilling Engineering Company Limited, China National Petroleum Corporation (CNPC), Hami, 839009, Xinjiang, China
[d] Department of Oil and Gas Technologies, Perm National Research Polytechnic University, Perm, 614990, Russia
[e] Fracture & Acidizing Technical Center, Research Institute of Petroleum Exploration and Development, PetroChina, Beijing, 100083, China

ARTICLE INFO

*Article history:*
Received 21 January 2022
Received in revised form
20 May 2022
Accepted 24 May 2022
Available online 27 May 2022

Edited by Yan-Hua Sun

*Keywords:*
Refracturing
Stress reorientation
Extended finite element method
Carbonate reservoir
Fracture diversion

ABSTRACT

Refracturing treatment is often performed on Russian carbonate reservoirs because of the quick production decline of reservoirs. The traditional refracturing model assumes that a refracture initiates in the normal direction relative to the initial hydro-fracture. This assumption is inconsistent with oilfield measurements of refracture propagation trajectories. Indeed, the existing model is not based on an in-depth understanding of initiation and propagation mechanisms of the second hydraulic fractures during refracturing. In this study, we use the extended finite element method to investigate refracture propagation paths at different initiation angles. Both the enriched function approach and phantom mode technique are incorporated into the refracturing model, thereby ensuring that the refracture can freely extend on the structured mesh without any refinement near the crack tips. Key factors including production time, stress anisotropy and initiation angle, and the propped mechanical effect are analyzed in detail. This study provides new insight into the mechanism of refracture propagation in unconventional reservoirs.



## 1. Introduction

When oil prices are low, refracturing treatment, which is a powerful technology to improve the production of unconventional oil and gas reservoirs, offers great economic advantages (Wright and Weijers, 2001; Xu et al., 2019; Yang et al., 2016). During refracturing, hydraulic fractures (i.e., refractures) propagate along the original hydraulic fracture's path or from a new direction due to stress changes induced by mechanical and poroelastic effects (Warpinski and Branagan, 1989; Palmer, 1993; Elbel and Mack, 1993; Roussel and Sharma, 2012). Refracture propagation paths constitute a trending topic in hydraulic fracturing.

There are two kinds of stimulation mechanisms in refracturing treatment. One mechanism is the rebirth of an old fracture. In other words, a refracture extends along the path of the original hydraulic fracture. This type of fracture propagation can enhance fracture conductivity and increase the drainage area. The other stimulation mechanism is stress reorientation or stress reversal (Warpinski and Branagan, 1989; Wright and Weijers, 2001; Li et al., 2017). The existence of proppant-filled fractures during initial fracturing (i.e., mechanical effect) and production-driven pore pressure depletion (i.e., poroelastic effects) lead to variation in the values of the two horizontal stresses and sometimes even the reversal of the stress field (Elbel and Mack, 1993; Wright and Conant, 1995; Siebrits et al., 2000). The inclination and azimuth of the new fracture differ from those of the original hydraulic fracture to varying degrees (Wright and Weijers, 2001). The extension of the new fracture into the unstimulated area increases the production of oil and gas wells.

As shown in Fig. 1, Siebrits et al. (1998) proposed a refracture propagation path based on the concept of a stress reversal region. The aforementioned mechanical effect and poroelastic effect are

* Corresponding author.
** Corresponding author.
*** Corresponding author.
**** Corresponding author.
*E-mail addresses:* upcwdb@bipt.edu.cn (D.-B. Wang), yubobox@vip.163.com (B. Yu), martyushevd@inbox.ru (D. Martyushev), lxfei@cup.edu.cn (X.-F. Liu).

https://doi.org/10.1016/j.petsci.2022.05.013

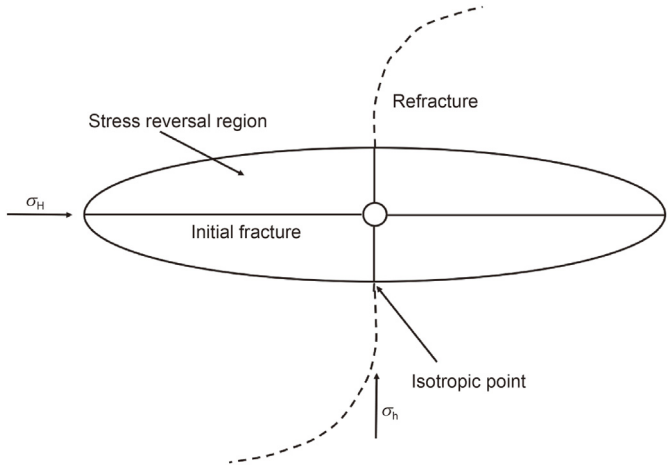


**Fig. 1.** Schematic diagram of fracture reorientation during refracturing.

due to the propped artificial fracture-induced stress field and production-induced stress field, respectively. The sum of the induced stress in the direction of the original maximum horizontal principal stress (denoted by $\Delta\sigma_x$) and $\sigma_H$ (i.e., $\sigma_H + \Delta\sigma_x$) is less than the sum of the induced stress in the direction of the original minimum horizontal principal stress ($\Delta\sigma_y$) and $\sigma_h$ (i.e., $\sigma_h + \Delta\sigma_y$). Refractures may thus initiate normal to the initial fracture before diverting into the direction of the original maximum horizontal principal stress. Thus, refracture propagation paths are dependent on both propped hydraulic fracture-induced stress and production-induced stress.

Elbel and Mack (1993) established a two-dimensional mathematical model considering the fluid-solid coupling effect, and they studied the variation relationship between time and pore pressure around the initial artificial fracture. Their results showed that the long-term production practice easily changes the reservoir stress field. Berchenko and Detournay (1997) found analytical solutions to the stress reorientation problem induced by water injector. Their study showed that the shear stress induced by water injection/production may cause fractures between injection/production wells to divert to a water injection well. Zhai (2006) presented a poroelastic model for calculating the effect of fluid injection and production-induced stress on fracture reorientation during refracturing under a variety of conditions. The numerical results showed that both the far-field maximum and minimum horizontal stress are altered by the gradient of pore pressure. The key factors influencing fracture reorientation include ground stresses, mechanical properties of rock, and the gradients of pore pressure. Rock permeability, heterogeneity, and anisotropy are other factors influencing stress reorientation. The rock properties dictate the optimal time window for the orthogonal refracture to be formed during refracturing (Roussel and Sharma, 2010; Zhang and Chen, 2010).

As previously mentioned, a propped hydraulic fracture-induced stress field results from the mechanical opening of a hydro-fracture. Sneddon and Elliot (1946) proposed an analytical solution to the propped hydraulic fracture-induced stress field problem based on the assumption of plane strain in an elastic body. Calculations have shown that the induced stress increases as the net pressure in fractures increases (Warpinski and Branagan, 1989; Wang et al., 2015a). A field mini-frac test in an offset well showed that the stress changes due to propped hydraulic fractures are between 1.7 and 2.1 MPa (Warpinski and Branagan, 1989). Refractures may initiate normal to the original fracture direction in coalbed methane wells if the original propped fractures have altered the maximum and minimum horizontal principal stresses sufficiently (Palmer, 1993). Numerical simulation showed that outside of the stress reversal region, the direction of the far-field maximum horizontal stress is along the direction of the original hydraulic fracture, unlike in the case of fluid production-induced stress (Roussel and Sharma, 2012).

There are many factors influencing refracture propagation, such as stress anisotropy, rock permeability, and the production rate. Siebrits et al. (1998) proposed three dimensionless parameters (i.e., dimensionless time, dimensionless stress deviator, and dimensionless toughness) to reduce the number of these influential factors. Among these dimensionless parameters, dimensionless toughness is used to determine the isotropic point at which the two horizontal stresses are equal. Based on damage mechanics theory, Li et al. (2017) developed a coupled poromechanical model to investigate stress redistribution during refracturing. They pointed out that pressure depletion and the Biot coefficient have positive correlations with the optimal refracturing time, while the horizontal stress ratio and Poisson's ratio have negative correlations with the time. Based on a new virtual internal bond method, Wang et al. (2021b) proposed a refracture propagation model which considers the time-dependent and stress-dependent behavior during refracturing. Chen et al. (2022) built up a refracturing model with a temporary plugging effect, and this effect is equivalent to the increase of dynamic viscosity of fracturing fluid in the cracked cohesive elements. By using this model, some cracked branch fractures can be well observed during refracturing in conglomerate reservoirs, which is in line with reality in field application. Refracturing laboratory experiments show that fracture complexity is related to the concentration of temporary plugging agents (Zhang et al., 2022). A relatively low concentration generates a bi-wing fracture, while a relatively high concentration is beneficial to forming complex fractures during refracturing.

Many refracturing models assume that a refracture initiates orthogonal to the initial hydraulic fracture according to the concept of the stress reversal zone (Zhang and Chen, 2010; Li et al., 2017; Zhang et al., 2021; Cong et al., 2022). However, both field measurements and laboratory experiments show that a refracture can initiate and propagate from an angle of inclination with respect to the initial hydraulic fracture (Wright, 1994; Wright and Conant, 1995; Wright and Weijers, 2001; Liu et al., 2008). Tiltmeter monitoring of five refracturing treatments showed that a refracture initiates at an angle between 30° and 60° with respect to the initial fracture, while monitoring of refracturing treatment in an infill well showed that a refracture initiates at an angle greater than 60° with respect to the initial fracture. Laboratory tests showed that the initiation angle of a refracture can change with respect to the initial fracture under different stress conditions (Liu et al., 2008; Shi et al., 2013; Wang et al., 2015b).

To the best of the authors' knowledge, existing research fails to provide an in-depth explanation of the initiation and propagation

mechanisms of the second hydro-fracture during refracturing. In this study, we use the extended finite element method (XFEM) to investigate refracture propagation paths at different initiation angles. Compared with the traditional finite method of linear elastic fracture mechanics, cracks by using XFEM can extend freely on the mesh, and the mesh near the crack tip does not need to be refined. Key factors including production time, stress anisotropy, and initial fracture length are analyzed in detail. This work provides new insight into the mechanism of refracture propagation in unconventional reservoirs.

## 2. Theory and methodology

### 2.1. Governing equations

Mathematical equations associated with refracturing problems include those of deformation and failure behaviour of rock, fluid seepage in porous media, and hydraulic fractures. The next sections provide the corresponding partial differential equations (PDEs) in detail.

#### 2.1.1. Rock deformation

We assume that rock deformation during hydraulic fracturing conforms to linear elastic theory. Considering Terzaghi's effective stress principle (Terzaghi, 1936), the equation for rock deformation can be written as

$$\nabla \cdot \boldsymbol{\sigma} = 0 \tag{1}$$

$$\boldsymbol{\sigma}'_{\text{eff}} = \boldsymbol{\sigma} + \alpha p \boldsymbol{I} \tag{2}$$

where $\boldsymbol{\sigma}'_{\text{eff}}$ is the tensor of effective stress; $\boldsymbol{\sigma}$ is the stress tensor; $\alpha$ is Biot's coefficient of effective stress; $p$ is the fluid pressure in the rock matrix; and $\boldsymbol{I}$ is the unit tensor.

#### 2.1.2. Seepage flow in the rock matrix

According to the law of conservation of mass in porous media, the continuity equation for seepage flow in rock matrix can be written as (Wang et al. 2020a, 2020b, 2021a)

$$\frac{1}{M}\dot{p} + \alpha \nabla \cdot \dot{\boldsymbol{u}} + \nabla \cdot \boldsymbol{v}_{\text{d}} = 0 \tag{3}$$

where $M$ is Biot's modulus; $\boldsymbol{u}$ is the displacement field of the rock matrix; and $\boldsymbol{v}_{\text{d}}$ is the flow velocity in porous media. The velocity is described by Darcy's law:

$$\boldsymbol{v}_{\text{d}} = -\frac{\boldsymbol{k}}{\mu}\nabla p \tag{4}$$

In Darcy's law, $\boldsymbol{k}$ is the rock-mass permeability tensor; and $\mu$ is fluid viscosity.

#### 2.1.3. Seepage flow in hydraulic fractures

Once the hydraulic fracture is generated in the formation, some of the fluid flows along the hydro-fracture, and the rest of the fluid leaks off into the rock matrix. Thus, the fluid flow in hydraulic fractures is expressed as (Wang et al., 2020b)

$$\dot{w} + \frac{\partial q}{\partial s} + q_{\text{L}} = 0 \tag{5}$$

where $w$ is the crack opening; $q$ is the flow rate in the hydraulic fractures, which is defined by the cubic law in Eq. (6); $s$ is the fracture location; and $q_{\text{L}}$ is the leak-off rate normal to the crack surface, which is expressed as the product of leak-off coefficient $c_{\text{L}}$ and the pressure difference between the hydraulic fracture and the rock matrix in Eq. (7). The equations are

$$q = -\frac{w^3}{12\mu}\frac{\partial p_{\text{f}}}{\partial s} \tag{6}$$

$$q_{\text{L}} = c_{\text{L}}\left(p_{\text{f}} - p_{\text{p}}\right) \tag{7}$$

where $p_{\text{f}}$ is the flow pressure in the hydraulic fracture; and $p_{\text{p}}$ is the fluid pressure in porous media.

### 2.2. Boundary conditions and variational forms

Fig. 2 depicts the computational domain (denoted as $\Omega$) with a propagating hydraulic fracture (Feng and Gray, 2019). The fracture surface is denoted as $\Gamma_{\text{d}}$. The unit normal vector $\boldsymbol{n}$ points outward to the fracture surface. The outer boundary of the domain is denoted as $\Gamma$, which consists of $\Gamma_{\text{u}}$, $\Gamma_{\text{p}}$, $\Gamma_{\text{t}}$, and $\Gamma_{\text{q}}$. On the outer boundary, there are two types of boundary conditions: the first boundary condition and the second boundary condition. The first boundary condition is expressed as shown in Eq. (8), which means that the constant displacement vector $\overline{\boldsymbol{u}}$ and pore pressure $\overline{p}$ are prescribed on the boundary segments $\Gamma_{\text{u}}$ and $\Gamma_{\text{p}}$, respectively. The second boundary condition is expressed as shown in Eq. (9), which means that the constant traction vector $\overline{\boldsymbol{t}}$ and flow rate $\overline{q}_{\text{w}}$ are prescribed on the boundary segments $\Gamma_{\text{t}}$ and $\Gamma_{\text{q}}$, respectively.

The boundary condition on the crack surface $\Gamma_{\text{d}}$ belongs to the Neumann boundary condition, as shown in Eq. (10). A net pressure is imposed on the crack surface $\Gamma_{\text{d}}$. This pressure is equal to the cohesive traction $\boldsymbol{t}^{\text{c}}$ minus the fluid pressure $p_{\text{f}}$ within the hydro-fracture. The normal flow rate between two fracture surfaces is denoted as $q_{\text{wd}}$ due to the leak-off behavior normal to the crack surface (c.f. Section 2.1.3). The symbol $[\![]\!]$ indicates the discrepancy between the nodal values of fluid velocity for the two fracture surfaces.

$$\begin{cases} \boldsymbol{u} = \overline{\boldsymbol{u}}, & \text{on } \Gamma_{\text{u}} \\ p = \overline{p}, & \text{on } \Gamma_{\text{p}} \end{cases} \tag{8}$$

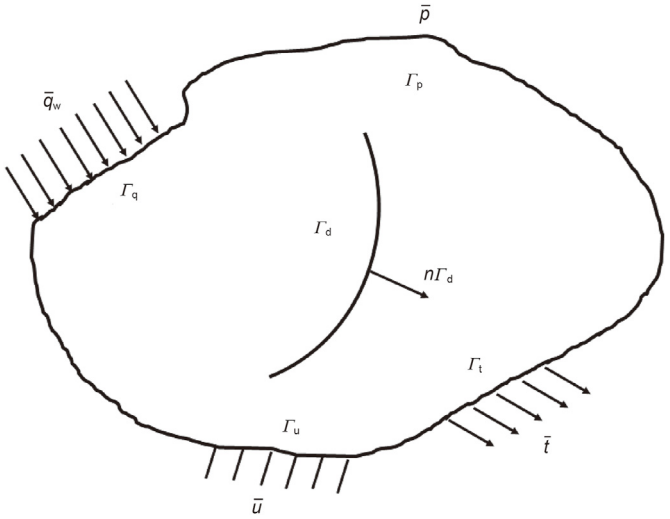


**Fig. 2.** Computational domain with a propagating hydraulic fracture and boundary conditions.

$$\begin{cases} \boldsymbol{\sigma}\cdot\boldsymbol{n} = \bar{\boldsymbol{t}}, & \text{on } \Gamma_{\mathrm{t}} \\ \boldsymbol{v}_{\mathrm{d}}\cdot\boldsymbol{n} = \bar{q}_{\mathrm{w}}, & \text{on } \Gamma_{\mathrm{q}} \end{cases} \tag{9}$$

$$\begin{cases} \boldsymbol{\sigma}\cdot\boldsymbol{n}_{\Gamma_{\mathrm{d}}} = \boldsymbol{t}^{\mathrm{c}} - p_{\mathrm{f}}\boldsymbol{n}_{\Gamma_{\mathrm{d}}} \\ [\![\boldsymbol{v}_{\mathrm{d}}]\!]\cdot\boldsymbol{n}_{\Gamma_{\mathrm{d}}} = q_{\mathrm{wd}} \end{cases} \tag{10}$$

Let us multiply test function $\boldsymbol{\eta}$ in Eq. (1) and integrate it on both sides. The weak form of the rock deformation equation is shown in Eq. (11), where $\nabla^{\mathrm{s}}$ is the symmetric operator of the gradient. It is noted that in Eq. (2), the total stress tensor $\boldsymbol{\sigma}$ should be replaced by Terzaghi's effective stress tensor $\boldsymbol{\sigma}'$.

$$\int_{\Omega}\nabla^{\mathrm{s}}\boldsymbol{\eta} : \boldsymbol{\sigma}\mathrm{d}\Omega + \int_{\Gamma_{\mathrm{d}}}[\![\boldsymbol{\eta}]\!]\cdot\left(\boldsymbol{t}^{\mathrm{c}} - p_{\mathrm{f}}\boldsymbol{n}_{\Gamma_{\mathrm{d}}}\right)\mathrm{d}\Gamma = 0 \tag{11}$$

Similar to the aforementioned mathematical transformation, test functions $\zeta$ and $\xi$ can be multiplied on both sides of Eq. (3) and Eq. (5), respectively. The weak forms of Eq. (3) and Eq. (5) are expressed in Eq. (12) and Eq. (13):

$$\int_{\Omega}\zeta\left(\frac{1}{M}\dot{p} + \alpha\nabla\cdot\dot{\boldsymbol{u}}\right)\mathrm{d}\Omega + \int_{\Omega}\frac{k}{\mu}\nabla\zeta\cdot\nabla p\mathrm{d}\Omega - \int_{\Gamma_{\mathrm{d}}}\zeta q_{\mathrm{wd}}\mathrm{d}\Gamma + \int_{\Gamma_{\mathrm{p}}}\zeta\bar{q}_{\mathrm{w}}\mathrm{d}\Gamma = 0 \tag{12}$$

$$\int_{\Gamma_{\mathrm{p}}}\xi\left(\dot{w} + \frac{\partial q}{\partial s} + q_{\mathrm{L}}\right)\mathrm{d}\Gamma + \int_{\Gamma_{\mathrm{p}}}\frac{\partial(\xi q)}{\partial s}\mathrm{d}\Gamma + \int_{\Gamma_{\mathrm{p}}}\frac{w^3}{12\mu}\frac{\partial p_{\mathrm{f}}}{\partial s}\frac{\partial\xi}{\partial s}\mathrm{d}\Gamma = 0 \tag{13}$$

The weak forms in Eq. (11) to Eq. (13) form a transient, non-linear, coupled fluid-solid system which includes rock deformation, fluid flow in porous media, and hydraulic fractures. The well-known Newton method is utilized to linearize the non-linear equations. An allowable time step is then determined to eliminate the numerical oscillation problem in Eq. (14):

$$\Delta t \geq \frac{\gamma_{\mathrm{F}}}{6Ek}(\Delta h)^2 \tag{14}$$

where $\Delta t$ is the time step, which is adaptive determination, and the variation range is between $1 \times 10^{-12}$ s and 5 s in this paper; $\Delta h$ is the mesh size, which is equal to 0.25 m in the XFEM simulation; $E$ is the modulus of elasticity of the rock matrix; $k$ is rock permeability; and $\gamma_{\mathrm{F}}$ is the specific gravity of the fluid.

Next, we describe in detail the discretization scheme of the coupled solid-fluid system and the fracture propagation criterion during hydraulic fracturing.

### 2.3. Cohesive traction-separation law

The cohesive traction-separation law has a clear advantage in fracture propagation problems. The law enables researchers to overcome the stress singularity of fracture tips by using the linear fracture mechanics (LEFM) theory. Fig. 3 depicts damage initiation and evolution in materials. Damage initiation means the start of the degradation of cohesive elements. In the XFEM of ABAQUS, the maximum principal stress criterion is often used to determine the initiation angle of the crack according to users' experiences (Haddad and Sepehrnoori, 2016). After damage initiation, the material enters the damage evolution process, which is defined as

$$t_{\mathrm{n}} = \begin{cases} (1-D)T_{\mathrm{n}}, & T \geq 0 \\ T_{\mathrm{n}}, & T < 0 \end{cases} \tag{15a}$$

$$t_{\mathrm{s}} = (1-D)T_{\mathrm{s}} \tag{15b}$$

where $D$ is damage factor; $t_{\mathrm{n}}$ and $t_{\mathrm{s}}$ denote the normal and shear traction components for the current separation with some amount of damage, respectively; and $T_{\mathrm{n}}$ and $T_{\mathrm{s}}$ denote the normal and shear stress components for the current separation without damage, respectively. The area of the triangle in Fig. 3 denotes the critical fracture energy release rate $G^{\mathrm{c}}$, which can be converted based on fracture toughness using Irwin's formula.

The damage factor has a relationship with the cohesive separation law:

$$D = \frac{\delta^{\mathrm{f}}\left(\delta^{\max} - \delta^0\right)}{\delta^{\max}\left(\delta^{\mathrm{f}} - \delta^0\right)} \tag{16}$$

$$\delta_{\mathrm{m}} = \sqrt{\delta_{\mathrm{n}}^2 + \delta_{\mathrm{s}}^2} \tag{17}$$

where $\delta^{\mathrm{f}}$ and $\delta^0$ are the effective separations that correspond to complete failure and damage initiation, respectively; and $\delta^{\max}$ and $\delta^{\mathrm{m}}$ are the maximum separation during the overcall loading process and the mean effective separation, respectively. In ABAQUS, Benzeggagh and Kenane's (1996) law, also known as the BK law, is adopted to simulate the fracturing process during hydraulic

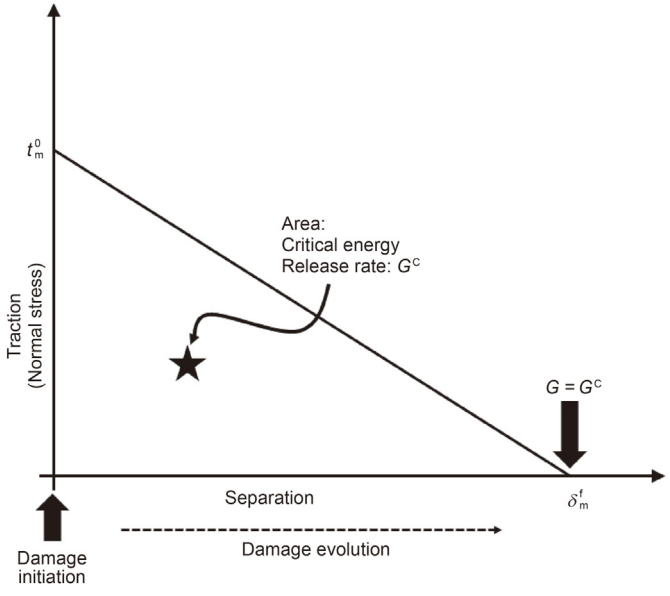


**Fig. 3.** Linear traction-separation law.

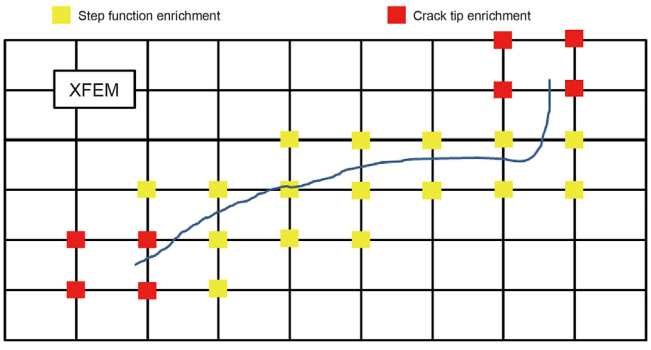


**Fig. 4.** XFEM enrichment functions of a fracture surface and fracture tips.

fracturing.

### 2.4. XFEM enrichment functions

Unlike the conventional finite element method, XFEM incorporates enrichment functions into its standard shape functions (Haddad and Sepehrnoori, 2016), as shown in Fig. 4. The XFEM enrichment functions include the step enrichment function for an element cut by the fracture surface and the crack tip enrichment function for an element including the crack tip. In the XFEM of ABAQUS, the crack tip enrichment is ignored to reduce the computation cost. Thus, the enrichment displacement field in ABAQUS is expressed as

$$\boldsymbol{u}(\boldsymbol{x}) = \sum_{i\in S_{\text{all}}} N_i(\boldsymbol{x})\boldsymbol{u}_i + \sum_{j\in S_{\text{frac}}} N_j(\boldsymbol{x})\boldsymbol{u}_i \left[H\left(f\left(x\right)\right) - H\left(f\left(x_j\right)\right)\right]\boldsymbol{a}_j \tag{18}$$

where $S_{\text{all}}$ and $S_{\text{frac}}$ are the node set including all the nodes and the node set cut by the fracture surface, respectively; $\boldsymbol{N}_i(\boldsymbol{x})$ and $\boldsymbol{N}_j(\boldsymbol{x})$ are the standard shape functions for $i \in S_{\text{all}}$ and $j \in S_{\text{frac}}$, respectively; $\boldsymbol{u}_i$ is the nodal values of the displacement vector; $\boldsymbol{a}_j$ is the degree of freedom (DOF) of the enriched elements; $H(\boldsymbol{x})$ is the Heaviside step function, which has the value of either 1 or −1, as shown in Eq. (19); $\boldsymbol{x}$ is a sample point; $\boldsymbol{x}^*$ is the point on the fracture surface that is the nearest to the point $\boldsymbol{x}$; and $\boldsymbol{n}$ is the unit normal vector to point outward from the fracture to the surface.

$$H(\boldsymbol{x}) = \begin{cases} 1, & \text{if } (\boldsymbol{x}-\boldsymbol{x}^*)\cdot\boldsymbol{n} \geq 0 \\ -1, & \text{if } (\boldsymbol{x}-\boldsymbol{x}^*)\cdot\boldsymbol{n} < 0 \end{cases} \tag{19}$$

When an element is fractured, the phantom node technique is utilized to describe the discontinuity between the two fracture surfaces (Song et al., 2006). In this technique, the phantom node overlaps the original node, and the fractured element becomes two elements cut by the opened fracture, as shown in Fig. 5. Then, the enriched displacement vector is expressed as

$$\boldsymbol{u}(\boldsymbol{x},t) = \sum_{i\in S_1} N_i(\boldsymbol{x})\boldsymbol{u}_i^1 H(-f(\boldsymbol{x})) + \sum_{i\in S_2} N_i(\boldsymbol{x})\boldsymbol{u}_i^2 H(f(\boldsymbol{x})) \tag{20}$$

where $S_i$ is the node set of the overlapped element $i$; and $\boldsymbol{u}_i^j$ is the nodal DOF of the overlapped element $j$.

### 2.5. XFEM discretization scheme

The pore pressure is approximated as the product of the shape function of pressure $N(\boldsymbol{x})$ and the nodal pressure values $p_i$, which is expressed as

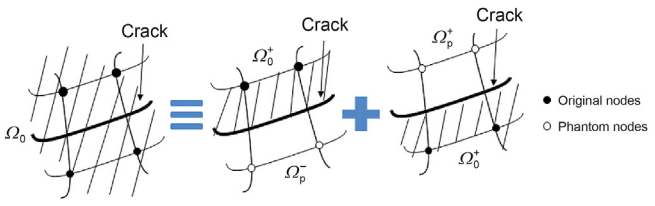


**Fig. 5.** Phantom node technique.

$$p(\boldsymbol{x}) = \sum_{i\in S_{\text{all}}} N(\boldsymbol{x})p_i \tag{21}$$

Next, we focus on the finite element discretization scheme of weak forms. Substituting the finite element approximation of the displacement vector and the pore pressure into the weak form of rock deformation, we obtain

$$\boldsymbol{f}^{\text{ext}} = \boldsymbol{f}^{\text{int}} + \boldsymbol{f}^{\text{pore}} + \boldsymbol{f}^{\text{fluid}} + \boldsymbol{f}^{\text{coh}} \tag{22}$$

where $\boldsymbol{f}^{\text{ext}}$ is the external force; $\boldsymbol{f}^{\text{int}}$ is the internal force; $\boldsymbol{f}^{\text{pore}}$ is the pore fluid force; $\boldsymbol{f}^{\text{fluid}}$ is the fracture fluid force; and $\boldsymbol{f}^{\text{coh}}$ is the cohesive contact force. The force vectors for the various elements are respectively expressed as (Song et al., 2006; Wang et al., 2017)

$$\boldsymbol{f}_{ei}^{\text{ext}} = \int_{\Gamma_{\text{t}}^e} \boldsymbol{N}^{\text{T}}\bar{\boldsymbol{t}}H\left((-1)^i f^e(\boldsymbol{x})\right)\text{d}\Gamma \tag{23}$$

$$\boldsymbol{f}_{ei}^{\text{int}} = \int_{\Omega^e} \mathbf{B}^{\text{T}}\sigma_e H\left((-1)^i f^e(x)\right)\text{d}\Omega \tag{24}$$

$$\boldsymbol{f}_{ei}^{\text{pore}} = \int_{\Omega^e} \alpha\boldsymbol{N}^{\text{T}}\frac{\partial p}{\partial \boldsymbol{x}}H\left((-1)^i f^e(x)\right)\text{d}\Omega \tag{25}$$

$$\boldsymbol{f}_{ei}^{\text{fluid}} = (-1)^i \int_{\Gamma_{\text{d}}^e} \boldsymbol{N}^{\text{T}}p\boldsymbol{n}\text{d}\Gamma \tag{26}$$

$$\boldsymbol{f}_{ei}^{\text{coh}} = (-1)^i \int_{\Gamma_{\text{d}}^e} \boldsymbol{N}^{\text{T}}\boldsymbol{t}^{\text{c}}\text{d}\Gamma \tag{27}$$

where $\boldsymbol{N}$ is the matrix of shape functions; and $\boldsymbol{B}$ is the derivative of the shape function of $\boldsymbol{N}$, and the mathematical expression of matrix $\boldsymbol{B}$ can be written as:

$$\mathbf{B} = \mathbf{SN} = \begin{bmatrix} \frac{\partial}{\partial x} & 0 \\ \frac{\partial}{\partial y} & 0 \\ \frac{\partial}{\partial y} & \frac{\partial}{\partial x} \end{bmatrix} \mathbf{N} \tag{28}$$

By neglecting the body force term, the discretization scheme of the fluid flow is expressed as (Nguyen et al., 2017; Wang et al., 2017)

$$\boldsymbol{C}\underline{\boldsymbol{p}} + \boldsymbol{Q}\underline{\boldsymbol{u}} + \boldsymbol{H}\boldsymbol{p} = \boldsymbol{f}_{\text{p}}^{\text{ext}} \tag{29}$$

$$\boldsymbol{C} = \int_{\Omega} \frac{1}{M}\boldsymbol{N}^{\text{T}}\boldsymbol{N}\text{d}\Omega \tag{30}$$

$$\boldsymbol{Q} = \int_{\Omega} \alpha(\nabla\boldsymbol{N})^{\text{T}}\cdot\boldsymbol{N}\text{d}\Omega \tag{31}$$

$$\boldsymbol{H} = \int_{\Omega} (\nabla \boldsymbol{N})^{\mathrm{T}} \cdot \kappa \cdot \nabla \boldsymbol{N} \mathrm{d}\Omega \tag{32}$$

$$\boldsymbol{f}_{\mathrm{p}}^{\mathrm{ext}} = \int_{\Gamma_{\mathrm{q}}} \boldsymbol{N}^{\mathrm{T}} \overline{q}_{\mathrm{w}} \mathrm{d}\Gamma \tag{33}$$

where $\kappa$ is the permeability coefficient. Combining the discretization scheme of Eq. (22) with Eq. (29), the numerical solution of the fully coupled fluid-solid system can be calculated using the ABAQUS standard solver.

## 3. Model verification

In order to verify our XFEM model, we solve two numerical examples by comparing our results to the published experimental results of hydraulic fracturing. A detailed description is presented in the next section.

### 3.1. Abass et al.'s laboratory fracturing experiment

Using the true tri-axial experiment system of hydraulic fracturing, Abass et al. (1994) observed fracture propagation in directional perforation wells. The size of the block is 0.15 × 0.15 × 0.25 $m^3$ with a 0.01-m radius wellbore in the center, as shown in Fig. 6a. The perforation length is equal to 0.0034 m with phase angles between 0 and 90°. The perforation density is 0.05 m for each interval. In the vertical direction, a 20.7 MPa stress (denoted as $S_v$ in Fig. 6a) is applied to the top of the block, and the two applied horizontal stress values are equal to 17.2 MPa (denoted as $S_H$ in Figs. 6a) and 9.6 MPa (denoted as $S_h$ in Fig. 6a), respectively. Fracturing fluid with a viscosity of 1.18 mPa s is pumped into the wellbore at an injection rate of 1.67 × $10^{-8}$ $m^3$/s. In this experiment, the pore pressure is equal to zero. The permeability and porosity of the rock sample are 9.5 mD and 0.33, respectively. The modulus of elasticity and Poisson's ratio of the rock sample are 17.4 GPa and 0.228, respectively. The fracture toughness is equal to 2500 kPa $m^{0.5}$. The tensile strength of the rock sample is equal to 5.56 MPa.

Based on the XFEM in ABAQUS, we construct a two-dimensional plane strain model to simulate hydraulic fracture propagation. The XFEM model includes 8968 CPE4P bilinear rectangular elements with pore pressure and 9120 nodes in the domain. We only simulate the case in which there is a 60° perforation angle from the wellbore because only the fracture morphology provided by Abass et al. (1994) is relatively clear. Thus, a pair of initial cracks, each 0.0034 m in length, is preset along a 60° inclined angle in the horizontal direction. The mesh near the wellbore must be refined to capture sufficiently accurate propagation trajectories during the simulation. Two steps including geostatic equilibrium and soil analysis are set up to simulate fracture propagation. The aforementioned three stresses in the vertical and horizontal directions are prescribed on the outer boundary. At the same time, a zero constant pore pressure is applied on the boundary.

The numerical simulation result is shown in Fig. 6b. This result is basically consistent with the propagation trajectories from Abass et al.'s (1994) experimental results. The weak inconsistency is due to rock heterogeneity. Thus, our XFEM model is relatively reliable.

### 3.2. Chen et al.'s experiment

Another verification model is compared with Chen et al.'s (2010) experimental results. The experiment uses a cubic 0.30 × 0.30 ×

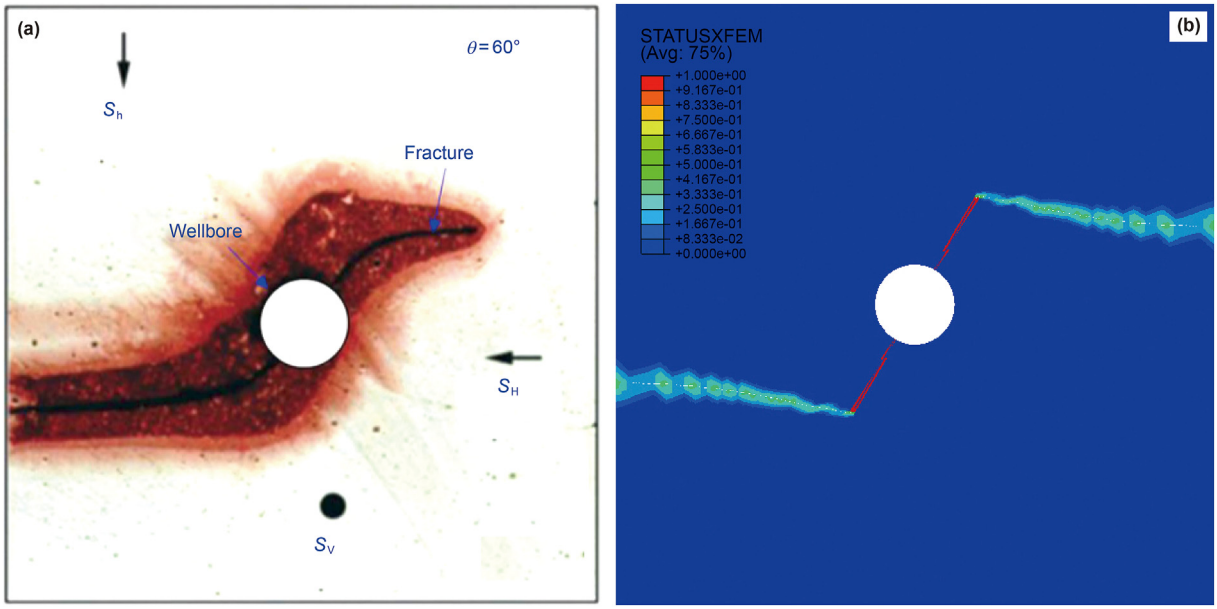


**Fig. 6.** Comparison between Abass et al.'s (1994) experimental results and the XFEM numerical simulation: (**a**) experimental results; (**b**) numerical simulation.

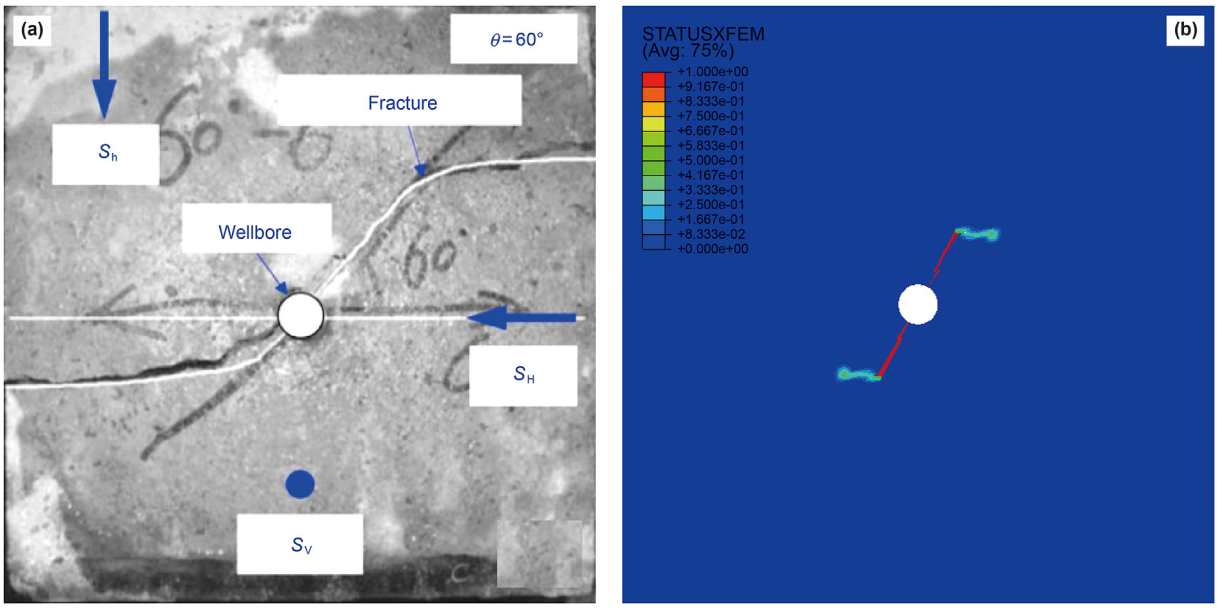


**Fig. 7.** Comparison between Chen et al.'s (2010) experimental results and XFEM numerical simulation: **(a)** experimental results; **(b)** numerical simulation.

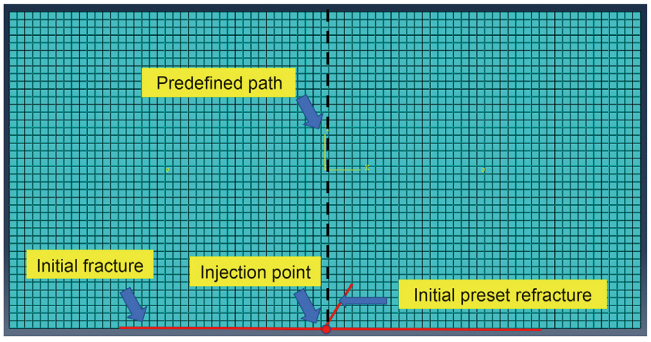


**Fig. 8.** XFEM refracturing model.

0.30 $m^3$ block (Fig. 7a). The rock sample is poured into cement for several days. A circular wellbore with a 0.01-m radius is drilled in the center after the six surfaces of the rock sample are polished. The vertical stress and two horizontal stresses applied to the rock surfaces are equal to 15, 6, and 1 MPa, respectively. The original pore pressure is neglected in this experiment. Fracturing fluid with a viscosity of 0.133 mPa s is injected to fracture the wellbore at a constant rate of $2.1 \times 10^{-9}$ $m^3$/s. The permeability and porosity of the rock sample are 0.1 mD and 0.185, respectively. The modulus of elasticity and Poisson's ratio of the rock sample are 8.4 GPa and 0.23, respectively. The fracture toughness is equal to 200 kPa $m^{0.5}$. The tensile strength of the rock sample is equal to 2.59 MPa.

Similar to the XFEM model in the previous section, this model yields numerical results that correspond nearly perfectly to the experimental fracture propagation path identified by Chen et al. (2010). This reaffirms the accuracy of our XFEM model (Fig. 7).

## 4. Numerical results

In this section, a numerical study is conducted to simulate the refracture propagation paths in Russian carbonate reservoirs. The oil and gas production occurs at the Famennian development site belonging to the Solikamsk depression in the Perm Krai (Martyushev and Yurikov, 2021; Novikov and Martyushev, 2020). The hydrocarbon production in carbonate reservoirs often decreases quickly after reaching its peak value in the early period of development due to hydrocarbon's strong heterogeneity and the closing of the fracture at high tectonic stresses. Thus, refracturing technology can recover the oil and gas production at a low oil cost.

### 4.1. Base case

As shown in Fig. 8, a $200 \times 100$ $m^2$ rectangle domain is modeled to denote a carbonate reservoir in Russia. This domain is divided into 3321 rectangular elements with pore pressure (CPE4P element in ABAQUS). The physical and mechanical parameters of the

**Table 1**
Mechanical and physical parameters of XFEM refracturing model.

| Parameter | Value | Parameter | Value |
|---|---|---|---|
| Permeability, mD | 3.042 | Vertical stress, MPa | 48.2 |
| Porosity | 0.11 | Maximum horizontal stress, MPa | 12.8 |
| Elastic modulus, GPa | 22.5 | Minimum horizontal stress, MPa | 7.45 |
| Poisson's ratio | 0.21 | Tensile strength, MPa | 1.4 |
| Fracture toughness MPa $m^{1/2}$ | 1.08 | Injection rate, $m^2$/min per reservoir thickness | 0.167 |
| Initial pore pressure, MPa | 12.21 | Layer thickness, m | 16.2 |
| Fluid viscosity, mPa s | 1.16 | Leak-off coefficient, m/(Pa s) | $1.64 \times 10^{-13}$ |
| Half-length, m | 50 | Boit coefficient | 1 |
| Fracture width, mm | 2 | Fluid compressibility, $Pa^{-1}$ | $1.7 \times 10^{-9}$ |

carbonate reservoir are shown in Table 1. To reduce the calculation burden, the semi-symmetric finite element model is adopted in the simulation. Thus, the initial hydro-fracture is located on the bottom of the rectangular domain with a half-length of 50 m, which corresponds to the red line at the bottom edge in Fig. 8. The injection point is at mid-edge of the bottom boundary. To simulate the refracture propagation after some production time, an initial crack is preset with different initiation angles relative to the horizontal direction (i.e., 15°/30°/45°/60°/90°). The angle is 15° in the base case. The constant displacement boundary conditions are imposed on the initial hydro-fracture to present the propped mechanical effect. The initial fracture width is set to be 2 mm on the red line in Fig. 8. Meanwhile, outer boundaries without the initial fracture are imposed on the vertical stress and two horizontal stresses, where the constant pore pressure is also imposed. The XFEM refracturing model includes three steps: geostatic equilibrium, production after initial fracturing, and refracturing treatment. It should be noted that the injection rate is positive when the well is produced, and the injection rate is negative when the well is refractured. In addition, we use the dimensionless time proposed by Siebrits et al. (2000) to reduce some ambiguities in the process of analysis, which is defined as

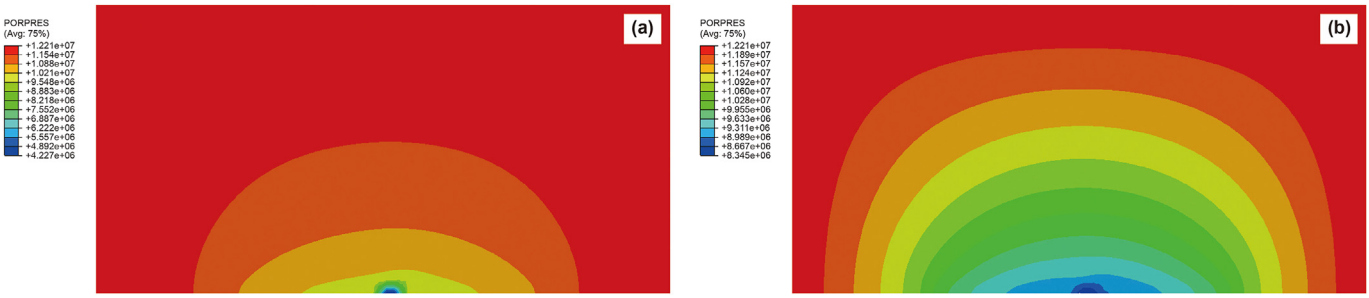


**Fig. 9.** Distribution contours of pore pressure around the initial fracture at different dimensionless times: **(a)** $\tau = 0.016$; **(b)** $\tau = 0.093$.

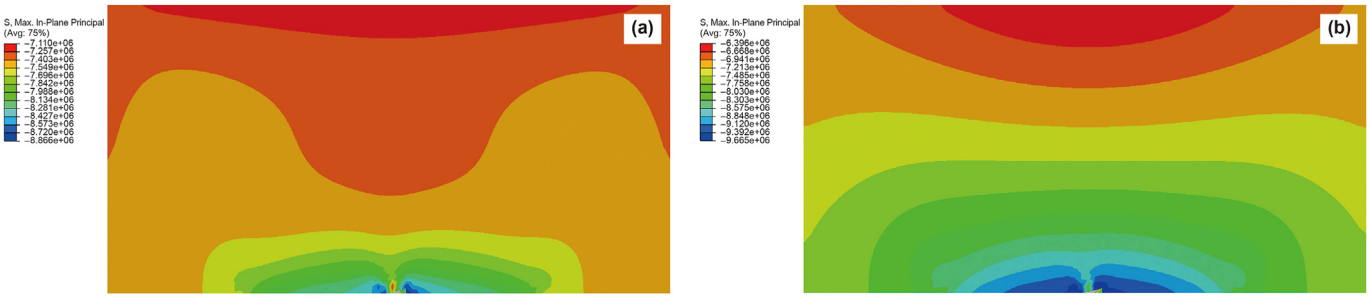


**Fig. 10.** Distribution contours of maximum principal stress around the initial fracture at different dimensionless times: **(a)** $\tau = 0.016$; **(b)** $\tau = 0.093$.

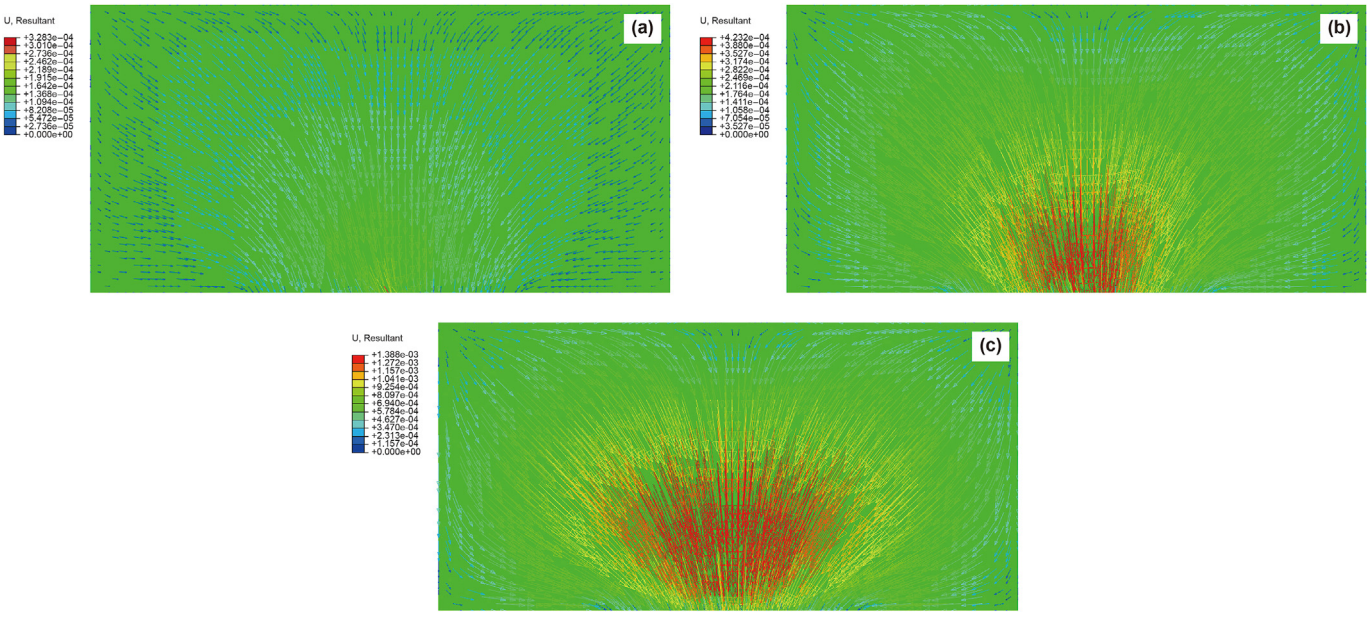


**Fig. 11.** Variation in stress reversal zone at different dimensionless times: **(a)** $\tau = 0.014$; **(b)** $\tau = 0.049$; **(c)** $\tau = 0.093$.

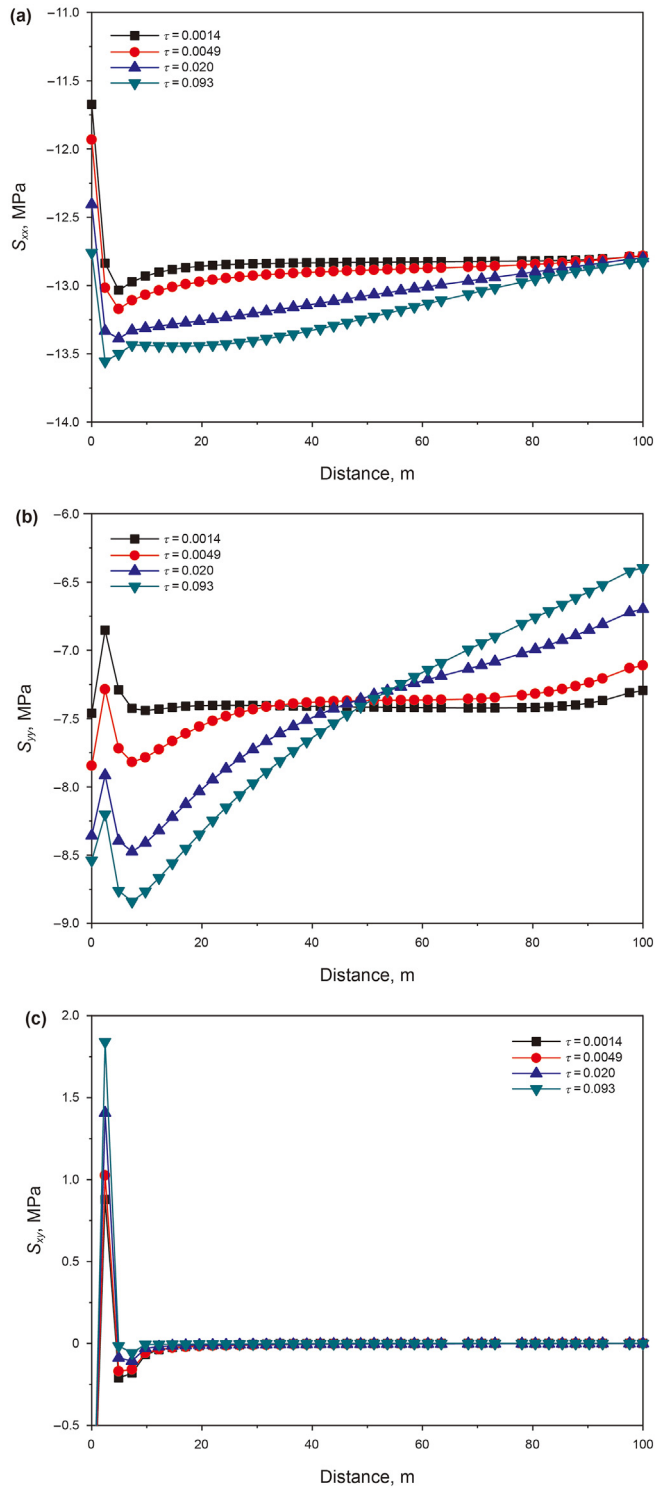


**Fig. 12.** Variation in stress components at different dimensionless times: **(a)** $S_{xx}$; **(b)** $S_{yy}$; **(c)** $S_{xy}$.

$$\tau = \frac{4kt}{\mu L_f^2\left[c_f\phi + \frac{\alpha_B(1+\upsilon)(1-2\upsilon)}{(1-\upsilon)E}\right]} \tag{34}$$

where $\tau$ is the dimensionless time; $E$ is the modulus of elasticity of carbonate rock; $\upsilon$ is Poisson's ratio; $k$ is rock permeability; $t$ is the production time; $c_f$ is fluid compressibility; $\alpha_B$ is the Biot coefficient; $\mu$ is the viscosity of injection fluid; and $L_f$ is the half-length of the initial hydro-fracture.

Fig. 9 depicts the distribution contours of pore pressure around the initial fracture at different dimensionless times. We observe the typically elliptical distribution of the pore pressure depletion. The size of the affected area increases as the dimensionless time increases. Fig. 10 depicts the contours of maximum principal stress around the initial fracture at different dimensionless times. We also observe that the numerical value of maximum principal stress varies with the dimensionless time, which is consistent with the analytical solution for induced stress found in previous work (Elbel and Mack, 1993; Siebrits et al., 2000; Wang et al., 2015a). This induced stress around the initial hydro-fracture is caused by the depleted pore pressure. In addition, the variation in the stress reversal zone at different dimensionless times is shown in Fig. 10. The result in Fig. 10 shows that the orientation of maximum principal stress around the initial hydro-fracture also changes with the production time. After an optimal time window, the original direction of the two horizontal principal stresses can be reversed (see Fig. 11).

In order to further investigate the relationship between the variation in the stress tensor around the initial fracture and the production time, we plot the corresponding curves along a predefined path, as shown in Fig. 8: i.e., the dotted black line in the vertical direction. Fig. 12 depicts the variation in three stress components (i.e., $S_{xx}$, $S_{yy}$, and $S_{xy}$) at different dimensionless times. We observe that both of the normal stress components along the path in Fig. 8, $S_{xx}$ and $S_{yy}$, are compressive stress and that the corresponding shear stress, $S_{xy}$, is almost tensile stress. With the increase in the dimensionless time, the absolute value of each of the stress components increases, which is due to the production-induced stress field around the initial hydro-fracture. In addition, the increment magnitude of $S_{yy}$ is greater than that of $S_{xx}$ because of the large space between these curves (Fig. 6b) at different dimensionless times. $S_{yy}$'s greater magnitude shows that the two horizontal principal stresses can be reversed after some production time. In addition, we observe that the magnitude of stress components undergoes major changes in locations that are less than 10 m from the initial fracture.

Fig. 13 depicts the refracture propagation paths with 2.35 MPa stress anisotropy at different dimensionless times. We observe that the refracture initiates from a 15° angle and diverts into the orientation of the original maximum principal stress in the case of a relatively low stress difference.

### 4.2. Initiation angle

The traditional theory of refracturing assumes that a refracture initiates perpendicular to the direction of the initial hydro-fracture. However, field measurements show that a refracture can initiate from different angles relative to the initial hydro-fracture (Wright and Weijers, 2001). Thus, we consider the scenario of refracture propagation at different angles, as shown in Fig. 14. The penetration length of the refracture is denoted as $L_{xf}'$, as shown in Fig. 1, which is the vertical distance from the isotropic point to the wellbore. We observe that the penetration length of the refracture increases as the initial angle increases. This shows that a 90° initiation angle is the most favorable because the refracture can penetrate and make contact with additional reservoirs normal to the direction of initial

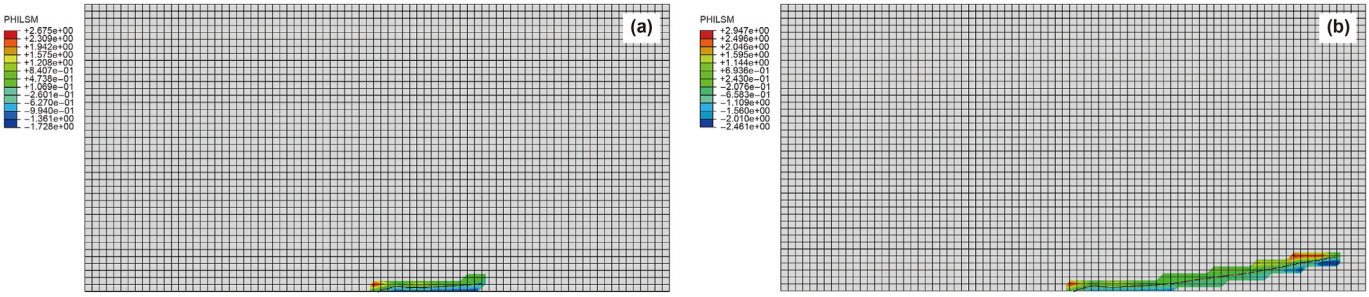


**Fig. 13.** Refracture propagation paths at different dimensionless times: **(a)** $\tau = 0.0029$; **(b)** $\tau = 0.0077$.

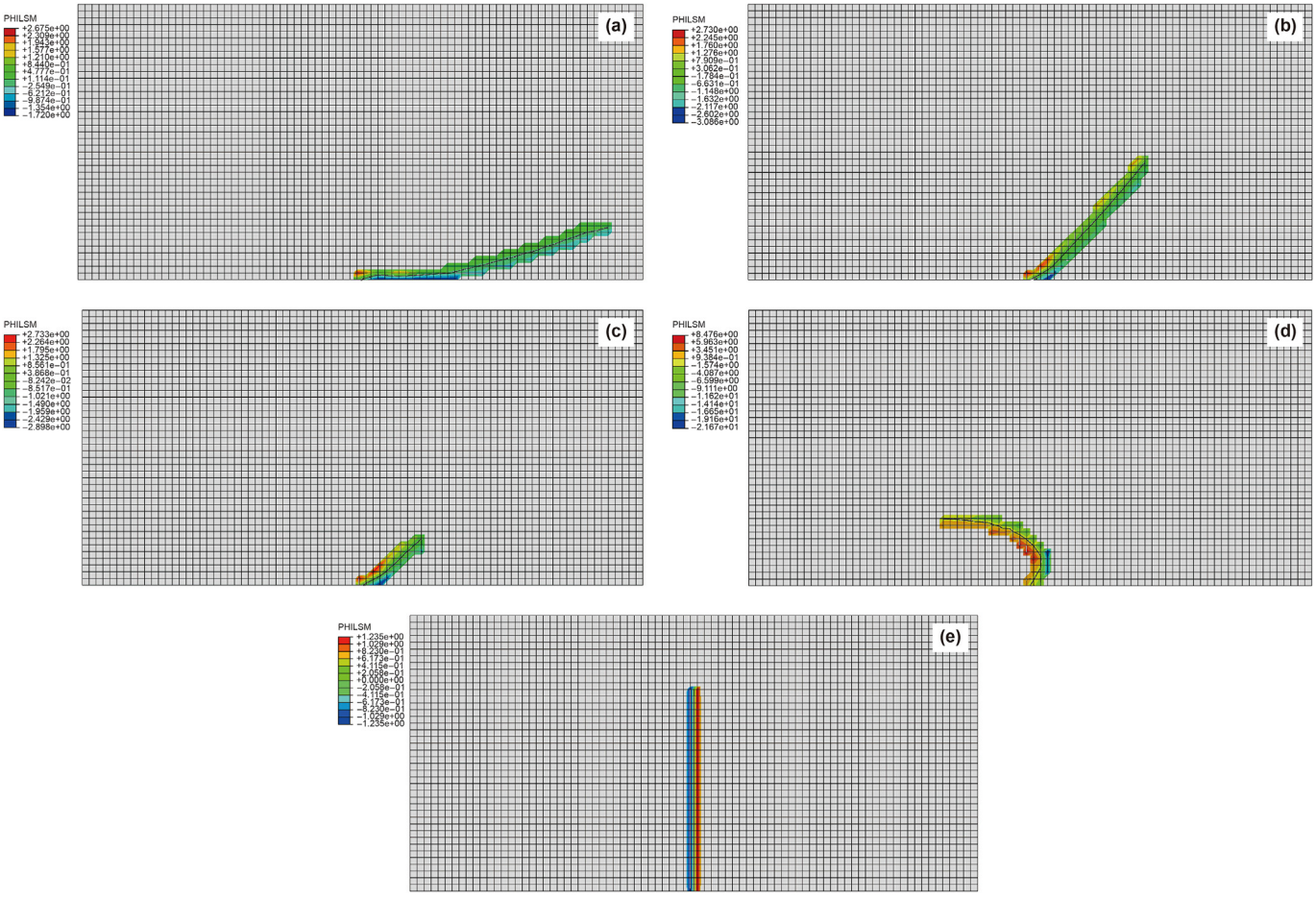


**Fig. 14.** Refracture propagation trajectories with a horizontal stress difference of 2.35 MPa at different initiation angles: **(a)** 15°; **(b)** 30°; **(c)** 45°; **(d)** 60°; **(e)** 90°.

fracture. Note that the refracture diverts into the left side of the domain in the case of a 60° angle, unlike in other cases. When the refracture initiates normal to the direction of initial hydro-fracture, the refracture propagates straight along the vertical direction and no diversion appears, as shown in Fig. 14e, due to the small stress anisotropy of 2.35 MPa. This shows that the penetration length of the refracture is long in the case of a 90° angle.

### 4.3. Stress anisotropy

Stress anisotropy is an important factor impacting fracture diversion in a rock formation. Figs. 15–18 depict refracture propagation trajectories with different initiation angles at different stress anisotropies. We observe that the penetration length of refracture propagation decreases as the stress anisotropy increases in each case of an initiation angle. Low stress anisotropy is favorable for refracturing treatment. With an increase in stress anisotropy, it

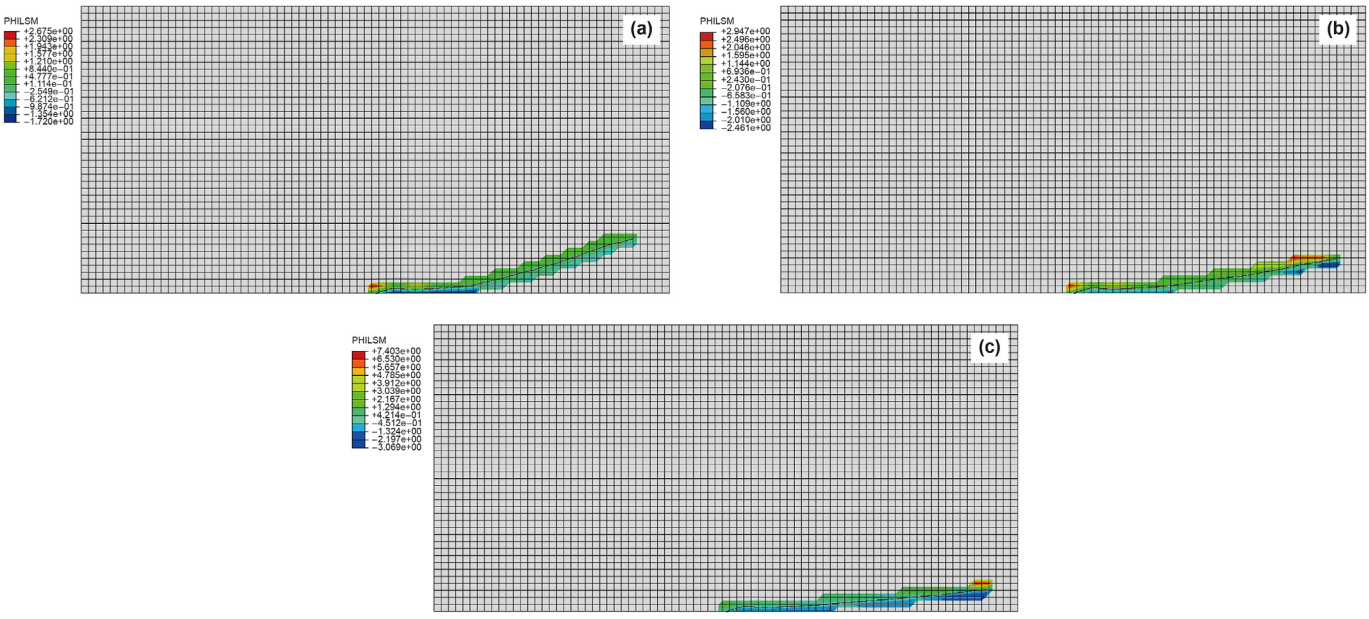


**Fig. 15.** Refracture propagation trajectories with a 15° initiation angle at different stress anisotropies: **(a)** 2.35 MPa; **(b)** 5.35 MPa; **(c)** 8.35 MPa.

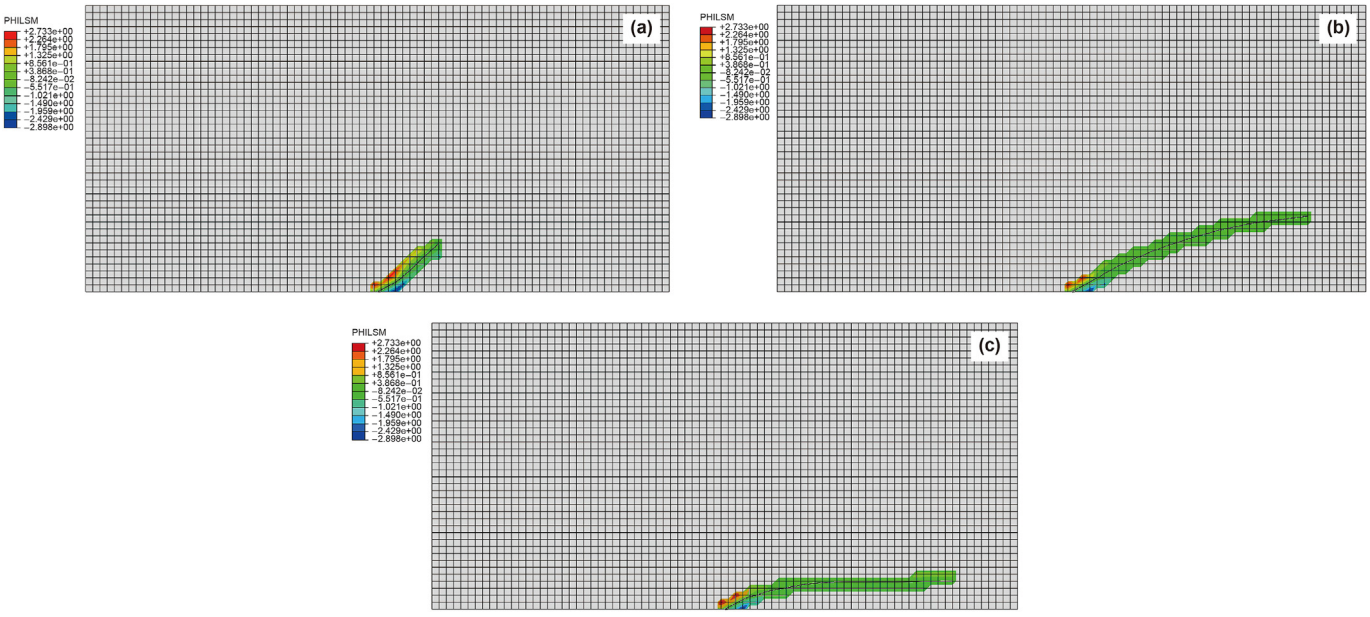


**Fig. 16.** Refracture propagation trajectories with a 45° initiation angle at different stress anisotropies: **(a)** 2.35 MPa; **(b)** 5.35 MPa; **(c)** 8.35 MPa.

becomes increasingly easy for the refracture to divert into the original maximum principal stress direction. Note that the refracture initiates and diverts into the left side of the domain, unlike in the case of a relatively small initiation angle. When the initiation angle reaches 90°, the refracture can divert into the left side or the right side of the domain. This shows that the refracture can initiate from either the left or right side of the domain, and the initiation direction is uncertain. This is a very special case of refracture propagation.

### 4.4. Production time

Production time can induce an additional stress field around the initial hydro-fracture due to the poroelasticity effect (Zhai, 2006; Wang et al., 2015a). It is the fluid entering/outflowing from the formation pores, which increases the pore pressure and causes formation dissolution, expansion, resulting in pore-elastic stress, thereby increasing the total stress, i.e., the fluid-induced stress field. The *in-situ* stress changes due to the diffusion of pore fluid

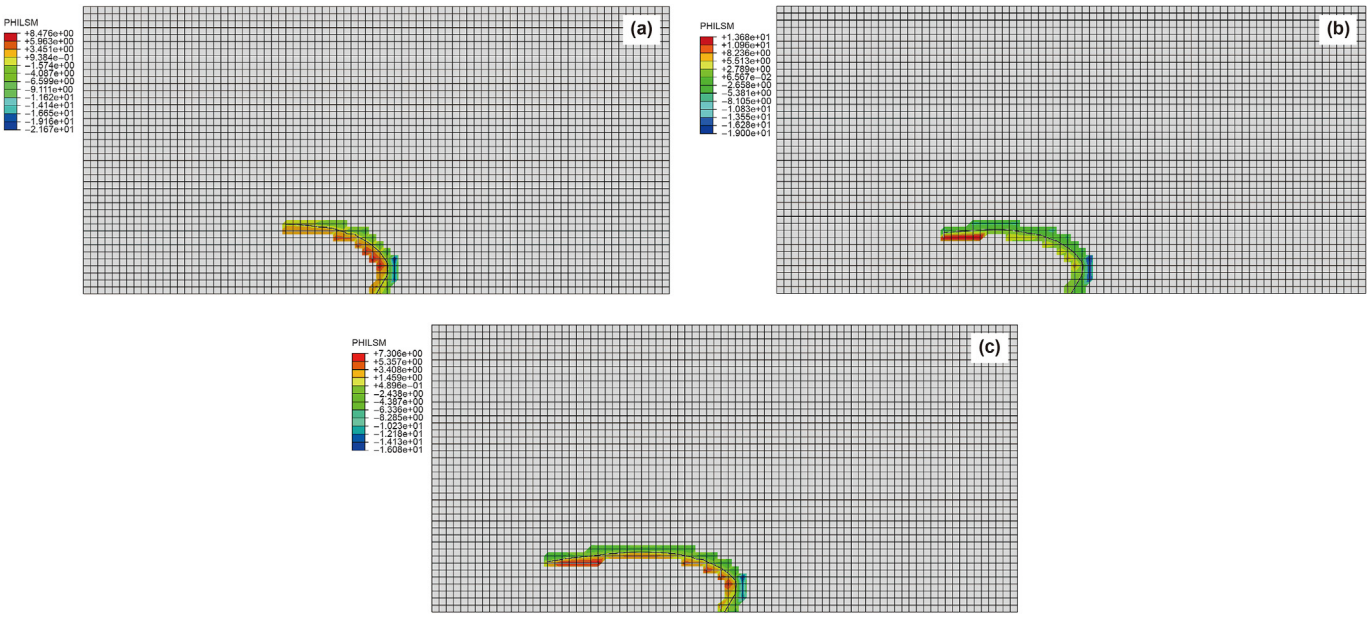


**Fig. 17.** Refracture propagation trajectories with a 60° initiation angle at different stress anisotropies: (**a**) 2.35 MPa; (**b**) 5.35 MPa; (**c**) 8.35 MPa.

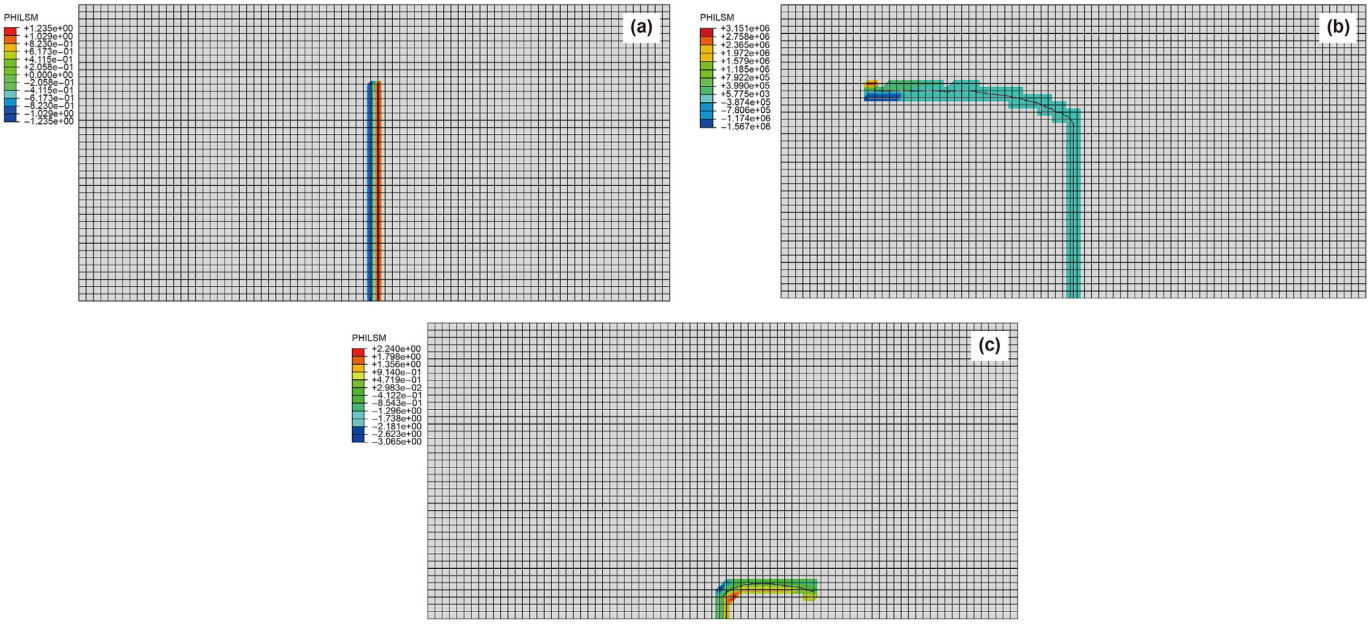


**Fig. 18.** Refracture propagation trajectories with a 90° initiation angle at different stress anisotropies: (**a**) 2.35 MPa; (**b**) 5.35 MPa; (**c**) 8.35 MPa.

into the bedrock. This phenomenon causes the stress intensity factor to change with time, and this change is an important factor governing the propagation of hydraulic fractures. In addition, when multiple wells are producing/injecting water, well spacing and inter-well interference can also affect the induced stress field caused by production. Fig. 19 and Fig. 20 depict refracture propagation paths at different dimensionless times with a 60° angle and 5.35 MPa/2.35 MPa stress anisotropies, respectively. Because of the stress state and the reservoir parameters, production time has no distinct effect on refracture propagation at various stress anisotropies.

### 4.5. Mechanical effect

An artificial fracture-induced stress field exists in the propped initial hydro-fracture due to the mechanical effect (Sneddon and Elliot, 1946; Warpinski and Branagan, 1989). We compare the results with and without the mechanical effect in the case of 2.35 MPa

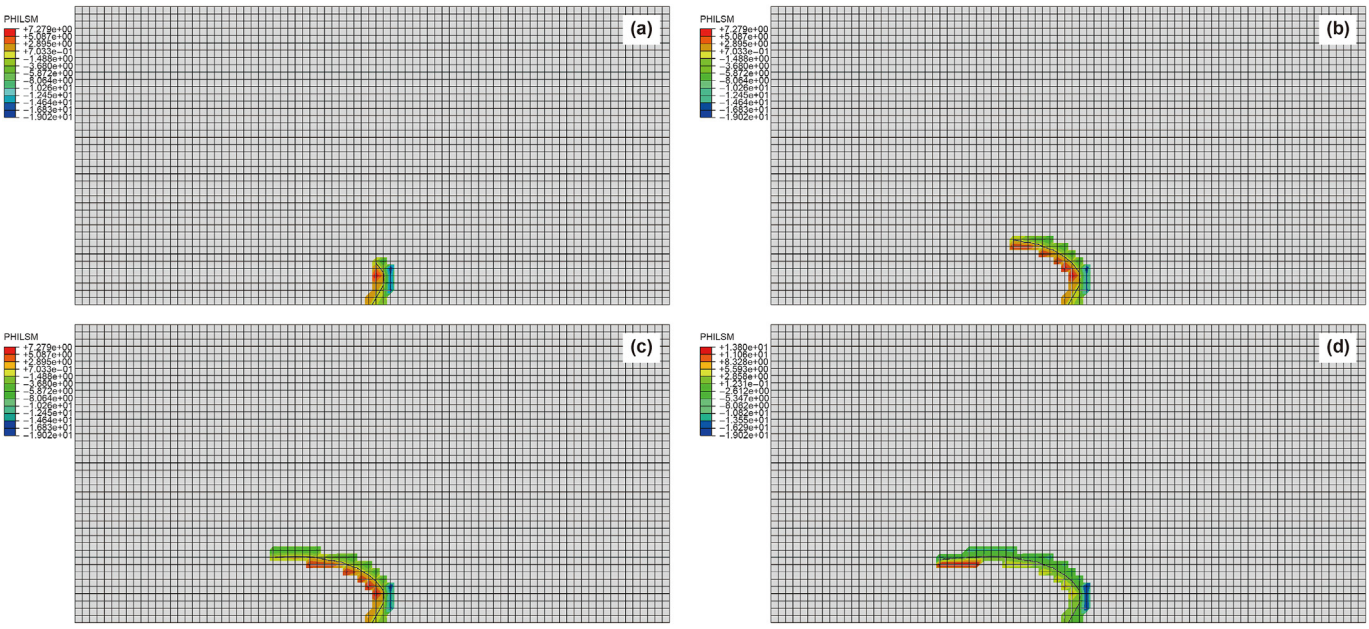


**Fig. 19.** Refracture propagation trajectories with a 60° initiation angle and 5.35 MPa stress anisotropy at different dimensionless times: (**a**) $\tau = 0.0037$; (**b**) $\tau = 0.074$; (**c**) $\tau = 0.093$; (**d**) $\tau = 0.111$.

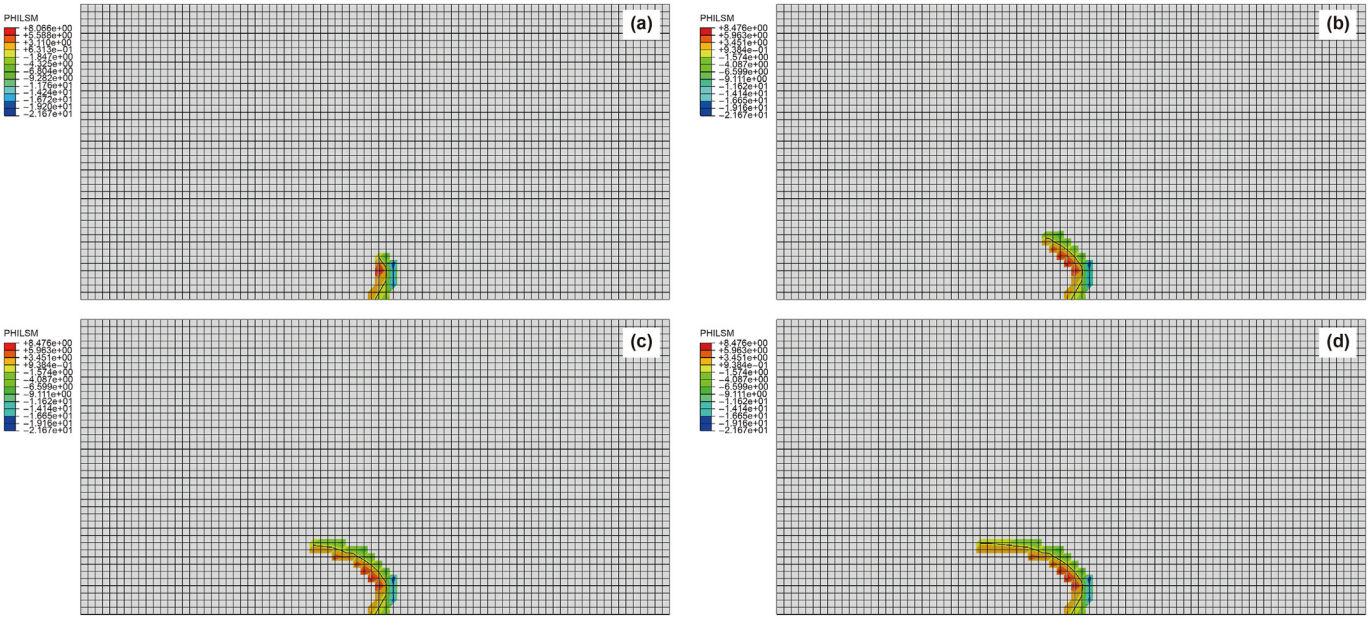


**Fig. 20.** Refracture propagation trajectories with a 60° initiation angle and 2.35 MPa stress anisotropy at different dimensionless times: (**a**) $\tau = 0.0019$; (**b**) $\tau = 0.0037$; (**c**) $\tau = 0.093$; (**d**) $\tau = 0.111$.

stress anisotropy, as shown in Fig. 21 and Fig. 22. We observe that the injection pressure is quite different in the two cases. The injection pressure with the mechanical effect causes an obvious pressure drop on the curve. Opening the new fracture requires more energy because of the stress concentration around the initial hydro-fracture. In addition, the refracture propagation paths with the mechanical effect (Fig. 22) are different from those without the mechanical effect (Figs. 19 and 20). The refracture diverts into the right side of the domain, while the refracture propagates along the left side of the domain. In addition, the penetration length of the refracture with the mechanical effect is shorter than that without the mechanical effect. These findings suggest that the mechanical effect is not beneficial for refracturing treatment because it limits the propagation distance in the vertical direction.

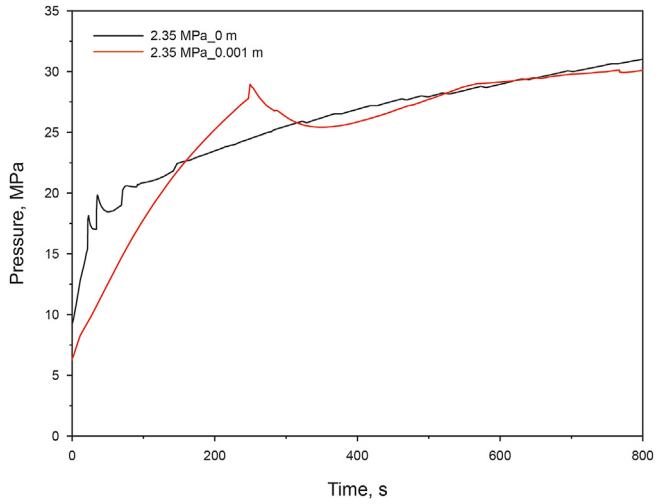


**Fig. 21.** Injection pressure comparison with and without the mechanical effect.

## 5. Discussion

The XFEM model in this study assumes the formation is homogeneous and isotropic. In fact, there are some natural fractures in subsurface. Besides, the temperature effect in the process of production is neglected. In deep formation, the thermal stress induced by production has obvious effect on stress reorientation. Some natural fractures can be open due to thermal expansion. Thus, this XFEM model has some limitations during the refracturing of naturally fractured reservoirs and deep formations. The mechanical behavior between hydraulic fractured and cemented natural fractures and the temperature effect induced by production should be incorporated into this XFEM model of refracturing as the next step.

## 6. Conclusions

Drawing on XFEM, this paper numerically investigated the mechanisms of fracture propagation during the refracturing of Russian carbonate reservoirs. Various factors influencing fracture propagation including the initiation angle, stress anisotropy, production time, and the mechanical effect were discussed in detail. Our main conclusions are as follows:

The parameters of the initiation angle, production time, stress difference, and the mechanical effect are the main factors influencing fracture propagation during refracturing.

In the case of the initiation angle, the smaller the horizontal stress difference is, the longer the diverting radius of the refracture is. This longer radius corresponds to the longer penetration length of the refracture in the vertical direction. The greater the horizontal stress difference is, the shorter the diverting radius of the refracture is, which is not beneficial for penetration in the vertical direction.

In the case of horizontal stress difference, the diverting radius of the refracture increases with the increase in the initiation angle, which is beneficial for penetration in the vertical direction.

Because of the stress state and the reservoir parameters, production time has no distinct effect on refracture propagation.

The mechanical effect has a significant effect on refracture propagation, and the propagation paths and injection pressure with and without the mechanical effect are quite different. The results show that the mechanical effect is not beneficial for penetration in the vertical direction during refracturing treatment.

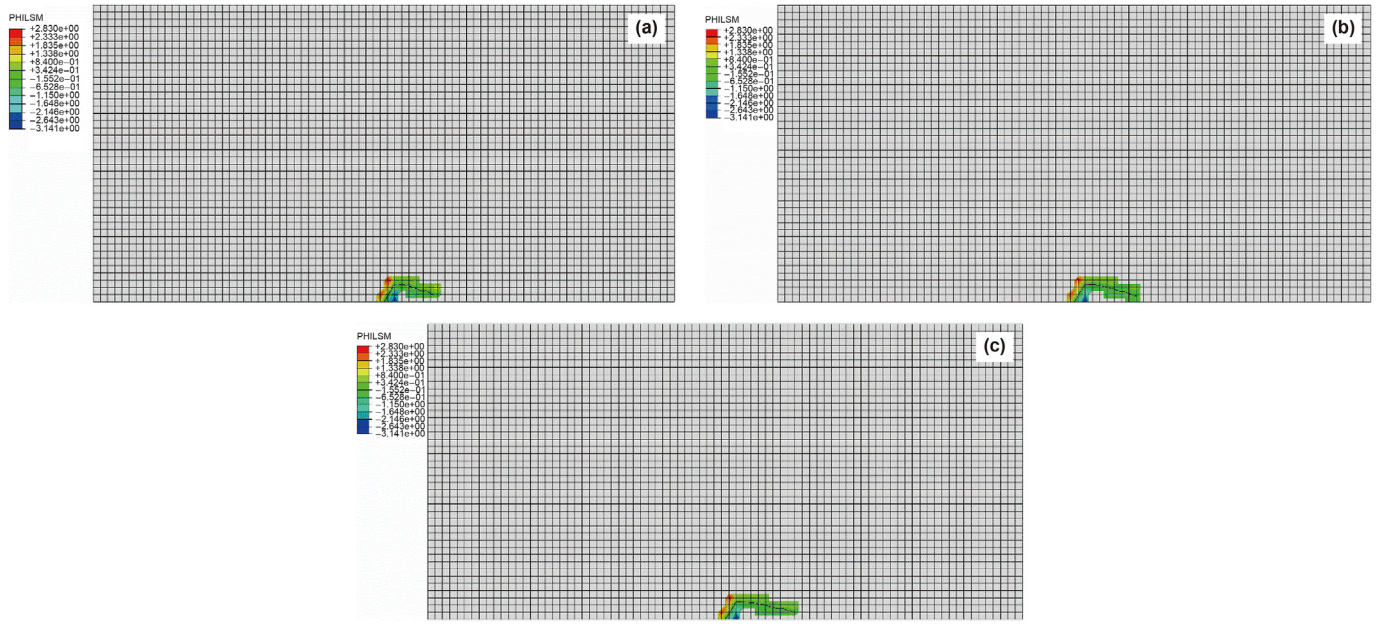


**Fig. 22.** Refracture propagation trajectories with a 60° initiation angle and 0.001 m mechanical effect at different stress anisotropies: (**a**) 2.35 MPa; (**b**) 5.35 MPa; (**c**) 8.35 MPa.

## Acknowledgments

This work was supported by Beijing Natural Science Foundation (Grant No. 3222030) and CNPC Innovation Found (Grant No. 2021DQ02-0201), the National Natural Science Foundation of China (Grant Nos. 51936001 and 52174045), and the Award Cultivation Foundation from Beijing Institute of Petrochemical Technology (Project No. BIPTACF-002).

## References

Abass, H.H., Brumley, J.L., Venditto, J.J., 1994. Oriented perforations - a rock mechanics view. SPE Annual Technical Conference and Exhibition. https://doi.org/10.2118/28555-MS.

Benzeggagh, M.L., Kenane, M., 1996. Measurement of mixed-mode delamination fracture toughness of unidirectional glass/epoxy composites with mixed-mode bending apparatus. Compos. Sci. Technol. 56 (4), 439–449. https://doi.org/10.1016/0266-3538(96)00005-X.

Berchenko, I., Detournay, E., 1997. Deviation of hydraulic fractures through poroelastic stress changes induced by fluid injection and pumping. Int. J. Rock Mech. Min. Sci. 34 (6), 1009–1019. https://doi.org/10.1016/S1365-1609(97)80010-X.

Chen, J., Zhang, Q., Zhang, J., 2022. Numerical simulations of temporary plugging-refracturing processes in a conglomerate reservoir under various in-situ stress difference conditions. Front. Phys. 9, 826605. https://doi.org/10.3389/fphy.2021.826605.

Chen, M., Jiang, H., Zhang, G.Q., Jin, Y., 2010. The experimental investigation of fracture propagation behavior and fracture geometry in hydraulic fracturing through oriented perforations. Pet. Sci. Technol. Taylor & Francis. 28 (13), 1297–1306. https://doi.org/10.1080/10916466.2010.483435.

Cong, Z., Li, Y., Pan, Y., Liu, B., Shi, Y., Wei, J., et al., 2022. Study on $CO_2$ foam fracturing model and fracture propagation simulation. Energy 238, 121778. https://doi.org/10.1016/j.energy.2021.121778.

Elbel, J.L., Mack, M.G., 1993. Refracturing: observations and theories. SPE Production Operations Symposium. https://doi.org/10.2118/25464-MS.

Feng, Y., Gray, K.E., 2019. XFEM-based cohesive zone approach for modeling near-wellbore hydraulic fracture complexity. Acta Geotech 14 (2), 377–402. https://doi.org/10.1007/s11440-018-0645-6.

Haddad, M., Sepehrnoori, K., 2016. XFEM-Based CZM for the simulation of 3D multiple-cluster hydraulic fracturing in quasi-brittle shale formations. Rock Mech. Rock Eng. 49 (12), 4731–4748. https://doi.org/10.1007/s00603-016-1057-2.

Li, X., Wang, J., Elsworth, D., 2017. Stress redistribution and fracture propagation during restimulation of gas shale reservoirs. J. Pet. Sci. Eng. 154, 150–160. https://doi.org/10.1016/j.petrol.2017.04.027.

Liu, H., Lan, Z., Zhang, G., Hou, F., He, X., Liu, X., 2008. Evaluation of refracture reorientation in both laboratory and field scales. SPE International Symposium and Exhibition on Formation Damage Control. https://doi.org/10.2118/112445-MS.

Martyushev, D.A., Yurikov, A., 2021. Evaluation of opening of fractures in the Logovskoye carbonate reservoir. Perm Krai, Russia. Pet. Res. 6 (2), 137–143. https://doi.org/10.1016/j.ptlrs.2020.11.002.

Nguyen, V.P., Lian, H., Rabczuk, T., Bordas, S., 2017. Modelling hydraulic fractures in porous media using flow cohesive interface elements. Eng. Geol. 225, 68–82. https://doi.org/10.1016/j.enggeo.2017.04.010.

Novikov, V., Martyushev, D., 2020. Acid treatment of carbonate deposits at the Perm Region oil fields. Perm Journal of Petroleum and Mining Engineering 20 (1), 72–87. https://doi.org/10.15593/2224-9923/2020.1.7.

Palmer, I.D., 1993. Induced stresses due to propped hydraulic fracture in coalbed methane wells. SPE Low Permeability Reservoirs Symposium. https://doi.org/10.2118/25861-MS.

Roussel, N.P., Sharma, M.M., 2010. Quantifying transient effects in altered-stress refracturing of vertical wells. SPE J 15 (3), 770–782. https://doi.org/10.2118/119522-PA.

Roussel, N.P., Sharma, M.M., 2012. Role of stress reorientation in the success of refracture treatments in tight gas sands. SPE Prod. Oper. 27 (4), 346–355. https://doi.org/10.2118/134491-MS.

Shi, Y., Zhou, F., Yang, X., Liu, X., Lian, S., Li, X., 2013. Laboratory study and field application of fiber-based fracture reorientation technology. International Petroleum Technology Conference. https://doi.org/10.2523/IPTC-16736-MS.

Siebrits, E., Elbel, J.L., Detournay, E., Detournay-Piette, C., Christianson, M., Robinson, B.M., et al., 1998. Parameters affecting azimuth and length of a secondary fracture during a refracture treatment. SPE Annual Technical Conference and Exhibition. https://doi.org/10.2118/48928-MS.

Siebrits, E., Elbel, J.L., Hoover, R.S., Diyashev, I.R., Griffin, L.G., Demetrius, S.L., et al., 2000. Refracture reorientation enhances gas production in Barnett shale tight gas wells. SPE Annual Technical Conference and Exhibition. https://doi.org/10.2118/63030-MS.

Sneddon, I.N., Elliot, H.A., 1946. The opening of a Griffith crack under internal pressure. Q. Appl. Math. 4 (3), 262–267. https://doi.org/10.1090/qam/17161.

Song, J.-H., Areias, P.M.A., Belytschko, T., 2006. A method for dynamic crack and shear band propagation with phantom nodes. Int. J. Numer. Methods Eng. 67 (6), 868–893. https://doi.org/10.1002/nme.1652.

Terzaghi, V.K., 1936. The shearing resistance of saturated soils and the angle between the planes of shear. 1st Int. Conf. Soil Mech. Found. Eng. 54–56.

Wang, D., Dong, Y., Sun, D., Yu, B., 2020a. A three-dimensional numerical study of hydraulic fracturing with degradable diverting materials via CZM-based FEM. Eng. Fract. Mech. 237, 107251. https://doi.org/10.1016/j.engfracmech.2020.107251.

Wang, D., Shi, F., Qin, H., Sun, D., Yu, B., 2021a. Failure patterns and mechanisms of hydraulic fracture propagation behavior in the presence of naturally cemented fractures. Comput. Model. Eng. Sci. 126 (3), 891–914. https://doi.org/10.32604/cmes.2021.014206.

Wang, D., Zhou, F., Ding, W., Ge, H., Jia, X., Shi, Y., et al., 2015a. A numerical simulation study of fracture reorientation with a degradable fiber-diverting agent. J. Nat. Gas Sci. Eng. 25, 215–225. https://doi.org/10.1016/j.jngse.2015.05.002.

Wang, D., Zhou, F., Ge, H., Shi, Y., Yi, X., Xiong, C., et al., 2015b. An experimental study on the mechanism of degradable fiber-assisted diverting fracturing and its influencing factors. J. Nat. Gas Sci. Eng. 27, 260–273. https://doi.org/10.1016/j.jngse.2015.08.062.

Wang, D., Zlotnik, S., Diez, P., Ge, H., Zhou, F., Yu, B., 2020b. A numerical study on hydraulic fracturing problems via the proper generalized decomposition method. Comput. Model. Eng. Sci. 122 (2), 703–720. https://doi.org/10.32604/cmes.2020.08033.

Wang, T., Liu, Z., Zeng, Q., Gao, Y., Zhuang, Z., 2017. XFEM modeling of hydraulic fracture in porous rocks with natural fractures. Sci. China Phys. Mech. Astron. 60 (8), 084612. https://doi.org/10.1007/s11433-017-9037-3.

Wang, Y., Zhao, B., Zhang, Z., 2021b. Numerical simulation of stress reorientation around wellbore in production and refracture stimulation. Eng. Anal. Bound. Elem. 133, 165–176. https://doi.org/10.1016/j.enganabound.2021.09.005.

Warpinski, N.R., Branagan, P.T., 1989. Altered-stress fracturing. J. Pet. Technol. 41 (9), 990–997. https://doi.org/10.2118/17533-PA.

Wright, C.A., 1994. Reorientation of propped refracture treatments in the lost hills field. In: SPE Western Regional Meeting. https://doi.org/10.2118/27896-MS.

Wright, C.A., Conant, R.A., 1995. Hydraulic fracture reorientation in primary and secondary recovery from low-permeability reservoirs. SPE Annual Technical Conference and Exhibition. https://doi.org/10.2118/30484-MS.

Wright, C.A., Weijers, L., 2001. Hydraulic fracture reorientation: does it occur? Does it matter? Lead. Edge. Society of Exploration Geophysicists 20 (10), 1185–1189. https://doi.org/10.1190/1.1487252.

Xu, T., Lindsay, G., Zheng, W., Baihly, J., Ejofodomi, E., Malpani, R., et al., 2019. Proposed refracturing-modeling methodology in the haynesville shale, a US unconventional basin. SPE Prod. Oper. 34 (4), 725–734. https://doi.org/10.2118/187236-PA.

Yang, L., Ge, H., Shi, X., Cheng, Y., Zhang, K., Chen, H., et al., 2016. The effect of microstructure and rock mineralogy on water imbibition characteristics in tight reservoirs. J. Nat. Gas Sci. Eng. 34, 1461–1471. https://doi.org/10.1016/j.jngse.2016.01.002.

Zhai, Z., 2006. Fracturing and Fracture Reorientation in Unconsolidated Sands and Sandstones. Ph.D. Dissertation. The University of Texas at Austin. https://repositories.lib.utexas.edu/handle/2152/3015.

Zhang, G.Q., Chen, M., 2010. Dynamic fracture propagation in hydraulic re-fracturing. J. Pet. Sci. Eng. 70 (3), 266–272. https://doi.org/10.1016/j.petrol.2009.11.019.

Zhang, J., Li, Y., Pan, Y., Wang, X., Yan, M., Shi, X., et al., 2021. Experiments and analysis on the influence of multiple closed cemented natural fractures on hydraulic fracture propagation in a tight sandstone reservoir. Eng. Geol. 281, 105981. https://doi.org/10.1016/j.enggeo.2020.105981.

Zhang, Y., Yu, R., Yang, W., Tian, Y., Shi, Z., Sheng, C., et al., 2022. Effect of temporary plugging agent concentration and fracturing fluid infiltration on initiation and propagation of hydraulic fractures in analogue tight sandstones. J. Pet. Sci. Eng. 210, 110060. https://doi.org/10.1016/j.petrol.2021.110060.